

# The Discovery of Radio Stars within 10'' of Sgr A\* at 7mm

F. Yusef-Zadeh<sup>1</sup>, D. A. Roberts<sup>1</sup>, H. Bushouse<sup>2</sup>, M. Wardle<sup>3</sup>, W. Cotton<sup>4</sup>, M. Royster<sup>1</sup>, & G. van Moorsel<sup>5</sup>

<sup>1</sup>*Department of Physics and Astronomy and CIERA, Northwestern University, Evanston, IL 60208*

<sup>2</sup>*Space Telescope Science Institute, Baltimore, MD 21218*

<sup>3</sup>*Dept of Physics and Astronomy, Macquarie University, Sydney NSW 2109, Australia*

<sup>4</sup>*National Radio Astronomy Observatory, Charlottesville, VA 22903*

<sup>5</sup>*National Radio Astronomy Observatory, Socorro, NM 87801*

## ABSTRACT

Very Large Array observations of the Galactic Center at 7 mm have produced an image of the 30'' surrounding Sgr A\* with a resolution of  $\sim 82 \times 42$  milliarcseconds (mas). A comparison with IR images taken simultaneously with the Very Large Telescope (VLT) identifies 41 radio sources with L-band ( $3.8 \mu\text{m}$ ) stellar counterparts. The well-known young, massive stars in the central Sgr A\* cluster (e.g., IRS 16C, IRS 16NE, IRS 16SE2, IRS 16NW, IRS 16SW, AF, AFNW, IRS 34W and IRS 33E) are detected with peak flux densities between  $\sim 0.2$  and  $1.3$  mJy. The origin of the stellar radio emission in the central cluster is discussed in terms of ionized stellar winds with mass-loss rates in the range  $\sim 0.8 - 5 \times 10^{-5} M_{\odot} \text{ yr}^{-1}$ . Radio emission from eight massive stars is used as a tool for registration between the radio and infrared frames with mas precision within a few arcseconds of Sgr A\*. This is similar to the established technique of aligning SiO masers and evolved stars except that radio stars lie within a few arcseconds of Sgr A\*. Our data show a scatter of  $\sim 6.5$  mas in the positions of the eight radio sources that appear in both the L-band and 7 mm images. Lastly, we use the radio and IR data to argue that members of IRS 13N are Young Stellar Objects rather than dust clumps, supporting the hypothesis that recent star formation has occurred near Sgr A\*.

*Subject headings:* Galaxy: center - galaxies: active - ISM: jets and outflows - stars: early type

## 1. Introduction

Most of the far-IR luminosity of the inner few pc of the Galactic Center (GC) region can be accounted for by the central cluster of emission-line stars distributed throughout the region (e.g.,

Gezari, Dwek & Varosi 2003; Genzel, Eisenhauer & Gillessen 2010). The central stellar cluster lies mainly within 1–10 arcseconds<sup>1</sup> of Sgr A\* and consists of about one hundred young massive OB and WR stars distributed amongst several small clusters, such as IRS 16 and IRS 13, within disks made up of stars (Paumard *et al.* 2006; Lu *et al.* 2009). Near-IR observations imply strong ionized winds with velocities on the order of 700 km s<sup>-1</sup> and a total mass-loss rate of  $4 \times 10^{-3} M_{\odot} \text{ yr}^{-1}$  (Martins *et al.* 2007) arising from the collection of the so-called disk stars in the central cluster. Sgr A\* is thought to be fuelled by partial capture of the winds from massive stars in the central cluster. The accretion rate was originally estimated from Br $\gamma$  line measurements, indicating mass-loss from individual cluster stars (Narayan *et al.* 1995; Coker & Melia 1997; Goldston *et al.* 2005; Falcke *et al.* 2009). The variability of the accretion rate was predicted by numerical simulations and analytical calculations accounting for the motion of individual mass-losing stars orbiting Sgr A\*, with the time averaged accretion rate was then estimated to be  $\sim 10^{-6} M_{\odot} \text{ yr}^{-1}$  (Quateart 2004; Cuadra *et al.* 2006, 2008). Radio emission from stars can potentially provide independent determination of mass-loss rates in the form of ionized stellar winds, with implications for the accretion rate onto Sgr A\*. In addition, these measurements can potentially identify the sites of the interaction of ionized stellar winds with gas near Sgr A\*, constraining physical parameters of the interstellar medium near the black hole. Radio observations, however, have so far been unable to identify isolated massive stars in the central cluster.

We present the highest resolution continuum image yet obtained of the inner 30'' of the GC at 7 mm. Previous high resolution 1.3 and 3.5 cm observations of this region were used to investigate the proper motion of HII regions (Yusef-Zadeh, Biretta & Roberts 1998; Zhao & Goss 1988; Zhao *et al.* 2009). Individual stellar sources could not be separated, however, from the ionized flow associated with orbiting gas (Zhao *et al.* 2009). Radio emission from ionized winds from young stars has already been detected from the Arches and Quintuplet clusters projected within 12' of Sgr A\* (Lang *et al.* 2005). The high resolution images presented here show for the first time radio emission from relatively isolated massive stars in the central stellar cluster centered on Sgr A\*. We determine the mass loss rate from ionized stellar winds to be quite similar to those in the Arches and Quintuplet clusters.

The positions of compact radio stars can also be used to precisely register the radio and IR frames within a few arcseconds of Sgr A\*. Aligning radio and IR frames is a technique that locates the position of the bright radio source Sgr A\* in highly confused IR images (Menten *et al.* 1997; Reid *et al.* 2003, 2007). This well-established technique uses maser emission from IR identified evolved stars to carry out accurate astrometry. Here we use the same technique and show that radio emission from hot stars can also be used for astrometric measurements. Precision astrometry using either radio stars or SiO masers has the potential in the search for post-Newtonian deviations in the stellar orbit of the S2 star located within 0.2'' of Sgr A\*. Lastly, a number of partially resolved radio sources have been detected toward IRS 13E and IRS 13N at 7mm. The sources in

---

<sup>1</sup>one arcsecond corresponds to 0.039 pc at the GC distance of 8 kpc

IRS 13N are thought to be dust clumps with embedded stars or YSOs. Here, we use 7mm data to argue that they are not dust clumps and that they support the YSO hypothesis.

## 2. Observations and Data Reduction

Detection of radio stars in the GC is not a trivial task. This is due to the crowded environment, where Sgr A\* and the extended ionized gas from the mini-spiral dominate the emission within the inner pc of Sgr A\*. Due to the bright diffuse emission from the mini-spiral, it is virtually impossible to unambiguously identify individual stellar sources in low resolution radio continuum images. An additional difficulty with identifying radio sources is the quadratic increase of the scattering size of distant sources with wavelength  $\lambda^2$  (e.g., Bower *et al.* 2006). To overcome these difficulties, we have conducted high resolution observations of the GC at 7 mm with the Very Large Array (VLA)<sup>2</sup>. These observations also have the advantage that radio emission from the ionized winds of hot stars has inverted spectrum ( $F_\nu \propto \nu^{0.6}$ ), and thus the emission is stronger at shorter wavelengths (Panagia & Felli 1975).

The VLA was used in its A configuration to carry out two pairs of observations at 7mm, each separated by one day, on July 8–9, 2011 and August 31–September 1, 2011. These high resolution observations used two IFs, 128 MHz wide, centered on 41.5 and 42.5 GHz. Each IF was composed of 64 channels, 2 MHz in width. J1331+3030 and J1744–3116 were used as the primary flux and complex gain calibrators, respectively. J1733–1304 was used to correct antenna pointing errors once every hour and was observed every ten minutes to calibrate complex gains and bandpass. Individual data sets were self-calibrated in phase and amplitudes to remove atmospheric phase errors. We fixed the average flux of Sgr A\* to be 2.2 Jy in each observation before 54 channels were combined and self-calibrated in both phase and amplitude. Due to the intrinsic variability of Sgr A\*, flux measurements taken from the combined radio image are uncertain by  $\sim 10 - 15\%$ . This is because the average flux of Sgr A\* was not the same in each session. The final image (Fig. 1) was constructed with a resolution of  $\sim 82 \times 42$  mas with an rms noise of 61  $\mu$ Jy per beam and a dynamic range of  $\sim 3.5 \times 10^4$ . The FWHM of the primary beam is 1' at 7 mm. The pair of observations is separated by 53 days from each other, so the effective epoch of the combined image is August 4, 2011. We employed background-subtracted 2D Gaussian fits using JMFIT in AIPS for measuring the properties of individual sources in the final radio image.

Eight sources were used to register the radio and IR images: IRS 16C, IRS 16NE, IRS 16NW, IRS 16SE2, IRS 33E, IRS 34W, AF, and AFNW (see Table 1). An L band ( $3.8\mu\text{m}$ ) image (Fig. 2) of the GC region was taken with the European Southern Observatory Very Large Telescope (VLT) on July 7, 2011. A color composite image using radio and IR data is shown in Figure 1b. The IR

---

<sup>2</sup>Karl G. Jansky Very Large Array (VLA) of the National Radio Astronomy Observatory is a facility of the National Science Foundation, operated under a cooperative agreement by Associated Universities, Inc.

image, shown in green in Figure 1b, is produced with the NaCo adaptive optics imager and covers a field of view of  $\sim 43''$ . The eight radio sources are relatively isolated and are easily distinguished from extended ionized gas, as can be seen in Figure 1a. The registration of the radio and IR images was accomplished as follows. The RA and Dec positions of the eight sources were measured in the radio map produced from the July 8, 2011 data by fitting elliptical Gaussians to the sources. The formal errors in the centroids of these measurements are on the order of 6 mas. Predicted x/y coordinates of the eight sources in the IR image were then computed by transforming the radio RA/Dec values into the IR image plane using the original World Coordinate System (WCS) definition of the IR image. We then measured the actual x/y positions of the eight sources in the IR image by fitting elliptical Gaussians with the IRAF/STSDAS task "n2gaussfit". The IR image is oversampled, with FWHM for point sources of  $\sim 4.4$  pixels, and a pixel scale of 0.0272 arcsec. The formal uncertainties of the centroids of the individual sources in the IR image are less than 1/100 of a pixel, or  $< 1$  mas. The predicted and measured x/y coordinates of the sources in the IR image were then used to compute a geometric transform between the radio and IR image spaces, using the IRAF task "geotran". The resulting transform was then applied to the IR image to assign a new World Coordinate System and ultimately to remap the IR image into the same WCS space as the radio image. The transform solution showed rms residuals to the fit of the eight source positions of  $\sim 6.5$  mas. We have measured positional errors of Sgr A\* before the data is self-calibrated. The error in the absolute position of Sgr A\* is estimated to be  $\sim 2.8$  mas. The total error in absolute position of radio stars when cross correlated with IR images is then estimated to be  $\sim 7.1$  mas. The residual errors in the positions of the eight sources in the IR image space are listed in Table 1 (column 5). The residuals are consistent with the uncertainty of the RA/Dec measurements in the radio image ( $\sim 6$  mas) and also must include an unknown component of uncertainty due to residual distortions in the construction of the mosaicked IR L-band image.

### 3. Results and Discussion

#### 3.1. Radio Stars

Figure 1a shows a grayscale version of the 7 mm radio image covering  $\sim 17'' \times 15''$  around Sgr A\*. The northern and eastern arm components of the extended mini-spiral components run to the NE and SE. The kinematics of these extended features indicate that they orbit Sgr A\* (e.g., Lacy *et al.* 1980; Roberts and Goss 1993; Zhao *et al.* 2009). We detect a large number of compact radio sources, as labeled on Figure 1a, within  $10''$  of Sgr A\*. Table 1 gives the IR identified names, RA and Dec coordinates (increasing in RA), total positional errors, residual astrometric errors, peak and integrated fluxes at 7 mm, the deconvolved beam angular sizes and the ID number for radio stars between 1 and 41. The flux measurements have accounted for the primary beam attenuation. The fitted position of Sgr A\* (ID 0) is also included in the Table. Several sources such as IRS 13E1, 13E2, 13E3, 13E5 and IRS 13N $\alpha$  to 13N $\gamma$  show radio counterparts. There are also stellar sources in these clusters that are not identified by name but have radio counterparts, as listed in

Table 1. To clarify radio sources with stellar counterparts in Table 1, we added a to k at the end of each cluster member. The effective epoch of these source detections taken from the combined 7 mm image, is August, 4, 2011. In table 1, the combined uncertainties in RA and Dec are listed in column 3 in mas for only nine sources. The remaining sources were either partially or fully resolved or too faint to get reasonable positional errors. Thus, the positional errors of these sources are not determined.

The nine radio stars coincide with some of the most luminous sources in the GC and the Galaxy as a whole (Paumard *et al.* 2006). Most of them show P-Cygni profiles, thus presenting strong evidence for stellar winds (Najarro *et al.* 1997; Martins *et al.* 2007). Although spectral index values of the radio stars are not available, the emission is most likely thermal, resulting from expanding ionized winds in the envelope of hot stars (Panagia & Felli 1975). We expect an insignificant contribution from nonthermal emission at 7 mm (Contreras *et al.* 1996).

We determined the mass-loss rate of individual radio stars assuming the standard model for a spherically-symmetric, homogeneous wind of fully ionized gas with  $T = 1 \times 10^4$  K and expanding with a constant terminal velocity (Panagia & Felli 1975). We assumed twice solar metallicity, a mean molecular weight  $\mu=2$  and adopted terminal velocities of IR stars, as given by Martins *et al.* (2007). Table 2 compares the mass-loss rates of several radio and IR stars, with rates determined from the radio measurements and from detailed model atmosphere calculations (Martins *et al.* 2007). Integrated fluxes and terminal velocities are also listed. IRS 16NE and IRS 16SW are binaries (Pfuhl *et al.* 2014), thus their model atmosphere calculations are not available. The mass-loss rates obtained using the radio and IR techniques agrees with each other to within a factor of two with the exception of IRS 33E. The mass loss rate of this star derived from radio measurements is a third of that from model atmosphere calculations given by Martin *et al.* (2007). This disagreement may reflect on the assumption that stellar winds are not clumpy and there is no nonthermal emission from radio stars. We note that mass-loss rate estimates are similar to those of radio stars in the Arches and Quintuplet clusters (Lang *et al.* 2005).

### 3.2. Radio and IR Astrometry

We selected eight of the nine hot stars for astrometric measurements. To determine if the detected radio sources have IR stellar counterparts, we used an L-band ( $3.8\mu\text{m}$ ) image which was taken on July 7, 2001. In order to register the L-band image with the VLA radio image, we matched eight stellar IR sources within about  $10''$  from Sgr A\* that are detected in the 7 mm radio map. Note that there should not be any offset in the position of stars due to proper motion because the radio and IR images were taken within one day of each other. The radio counterpart to IRS 16SW is in a confused region, so was not used in astrometric analysis. Figure 2 shows a larger view of the region shown in Figure 1 at  $3.8\mu\text{m}$  but with RA, Dec coordinates labeled. All 41 sources listed in Table 1 have IR counterparts. We have also detected radio star candidates with no IR counterparts.

Previous studies used the stellar SiO masers located beyond  $\sim 7''$  of Sgr A\* to register the radio and IR frames (Menten *et al.* 1997; Reid *et al.* 2003, 2007). This technique achieves positional accuracy of individual masers to  $\sim 1$  mas (Reid *et al.* 2007). Individual sources such as IRS 16NE show positional errors of 2.2 mas in the 7 mm radio image. Our approach of using radio stars to register the IR frame yields a statistical accuracy of the registration  $\sim 6.5$  mas. The eight radio stars used in our registration are distributed within  $\sim 10''$  of Sgr A\*. This registration has allowed us to cross-identify stellar sources in radio and infrared images.

### 3.3. Young Stellar Objects vs Dust Clumps

In addition to the hot mass-losing stars listed in Table 2, we detected multiple radio sources coincident with IR-identified stars and stellar clusters: 2 in IRS 1W, 4 in IRS 21, 6 in the IRS 13E cluster, 2 in IRS 5, and 11 in the IRS 13N cluster (Paumard *et al.* 2006; Lu *et al.* 2009; Maillard *et al.* 2004; Schödel *et al.* 2005; Muzic *et al.* 2008; Perger *et al.* 2008; Fritz *et al.* 2010; Eckart *et al.* 2004, 2013). Figure 3 shows 7 mm and L-band images of the IRS 13E and IRS 13N clusters located  $3.5''$  SW of Sgr A\*. IRS 13E consists of several early-type stars (e.g., Fritz *et al.* 2010; Eckart *et al.* 2013). Stellar sources IRS 16NE and IRS 16SW are binary systems and display evidence of X-ray emission resulting from colliding winds (Coker *et al.* 2002).

Unlike compact, hot stars, a number of radio sources are partially resolved, as shown in column 6 of Table 2. A significant deconvolved size of hot stars could not be measured, thus they are likely to be unresolved. By contrast, sources in the IRS 13N cluster, such as IRS 13N $\beta$  (source 23 in Table 1) have typical deconvolved beam sizes of  $77 \times 38$  mas. There is a debate as to whether some members of IRS 13E and IRS 13N clusters are dust clumps with embedded stars or Young Stellar Objects (YSOs; Muzic *et al.* 2008; Fritz *et al.* 2010; Eckart *et al.* 2013). There are two arguments against members of IRS 13N being dust clumps. First, IRS 13N has a flux density 1.34 Jy at  $3.8 \mu\text{m}$  (Viehmann *et al.* 2006), which yields a luminosity estimate  $4\pi d^2 \nu S_\nu = 6 \times 10^4 L_\odot$  after correcting for 2 magnitudes of extinction. If IRS 13N is a dust clump with no embedded source, we estimate a heating rate  $\sim \pi(400 \text{ AU})^2 * L_*/(4\pi (0.5 \text{ pc})^2) \sim 1200 L_\odot$ , assuming a typical distance of 0.5 pc from the GC, a source size of 800AU ( $0.1''$ ) and UV radiation field of corresponding to a luminosity  $L_* \approx 2 \times 10^7 L_\odot$  from the GC (Serabyn & Lacy 1985). The IR luminosity of IRS 13N exceeds the heating rate of IRS 13N by an order of magnitude. External heating by the intense stellar UV radiation field in the inner parsec of the galaxy, is insufficient, so an internal source of heating is needed. This favors the suggestion that these sources are dusty stars. Eckart *et al.* (2013) have made a number of arguments based on the motion of the IRS 16 cluster and the interstellar material surrounding the cluster that favor the young age of the IRS 13N cluster. We have also studied Spectral Energy Distribution (SED) fitting of IRS 13N which is consistent with a grid of model calculations of YSO candidates (Yusef-Zadeh *et al.* 2014, in preparation).

The second line of argument is that the radio emission is consistent with thermal bremsstrahlung from ionized gas that is being photo evaporated from a disk by the UV radiation field from hot stars

in the inner parsec of the Galaxy. The measured radio flux,  $\sim 2$  mJy at 43 GHz, implies a volume emission measure  $\int n_e^2 dV = 6 \times 10^{58} \text{ cm}^{-3}$ . Assuming a homogeneous source of  $\text{FWHM} \approx 0.1''$  and  $T_e = 8000$  K yields a source radius  $\sim 400$  AU and  $n_e \approx 2.5 \times 10^5 \text{ cm}^{-3}$ , with an optical depth  $\sim 0.02$ . The mass of ionized gas is then  $M_i \approx 3 \times 10^{-4} M_\odot$ . Hot stars in the inner parsec of the Galaxy do not create sufficient numbers of ionizing photons to explain this mass of ionized gas. The total production rate is estimated to be  $Q_{\text{LyC}} \approx 2.5 \times 10^{50} \text{ s}^{-1}$  (Genzel, Hollenbach & Townes 1994), implying an incident ionizing photon flux  $Q/(4\pi (1 \text{ pc})^2) \approx 2 \times 10^{12} \text{ s}^{-1} \text{ cm}^{-2}$ . This is in rough agreement with the hydrogen recombination rate per unit area in the ionized gas,  $\alpha^{(2)} n_e^2 r \approx 1 \times 10^{12} \text{ s}^{-1} \text{ cm}^{-2}$ . Assuming that the ionized gas expands at the sound speed  $c_s \approx 15 \text{ km s}^{-1}$  for  $T = 8000$  K, the mass-loss rate due to photo evaporation is  $M_i/(r/c_s) \approx 2.2 \times 10^{-6} M_\odot \text{ yr}^{-1}$ . This must be replenished on the expansion time scale  $r/c_s \approx 140$  yr, implying the existence of a reservoir of neutral material, presumably a disk associated with the YSO.

#### 4. Summary

We have detected a number of stellar sources within the inner  $10''$  of Sgr A\* in 7 mm radio continuum images with astrometric precision of  $\sim 6.5$  mas. The radio emission from GC stars is at a level consistent with ionized winds from hot massive stars with mass-loss rates determined from detailed modeling of the atmospheres. (Najarro *et al.* 1997; Martins *et al.* 2007). We also detected several radio sources in IRS 13N and IRS 13E suggesting that thermal radio emission from ionized gas is being photo-evaporated from disks of YSOs by UV radiation from hot stellar sources in the GC. This possibility is consistent with the idea that ongoing star formation is taking place within 0.5 pc of Sgr A\* (Eckart *et al.* 2013; Yusef-Zadeh *et al.* 2013).

This work is dedicated to L. Ozernoy who encouraged FYZ to search for ionized stellar winds at radio wavelengths in the mid 90's. We are grateful to S. Gillessen and the MPE group for providing us with a VLT image of the Galactic center. We thank the referee for detailed comments. This work is partially supported by the grant AST-0807400 from the NSF.

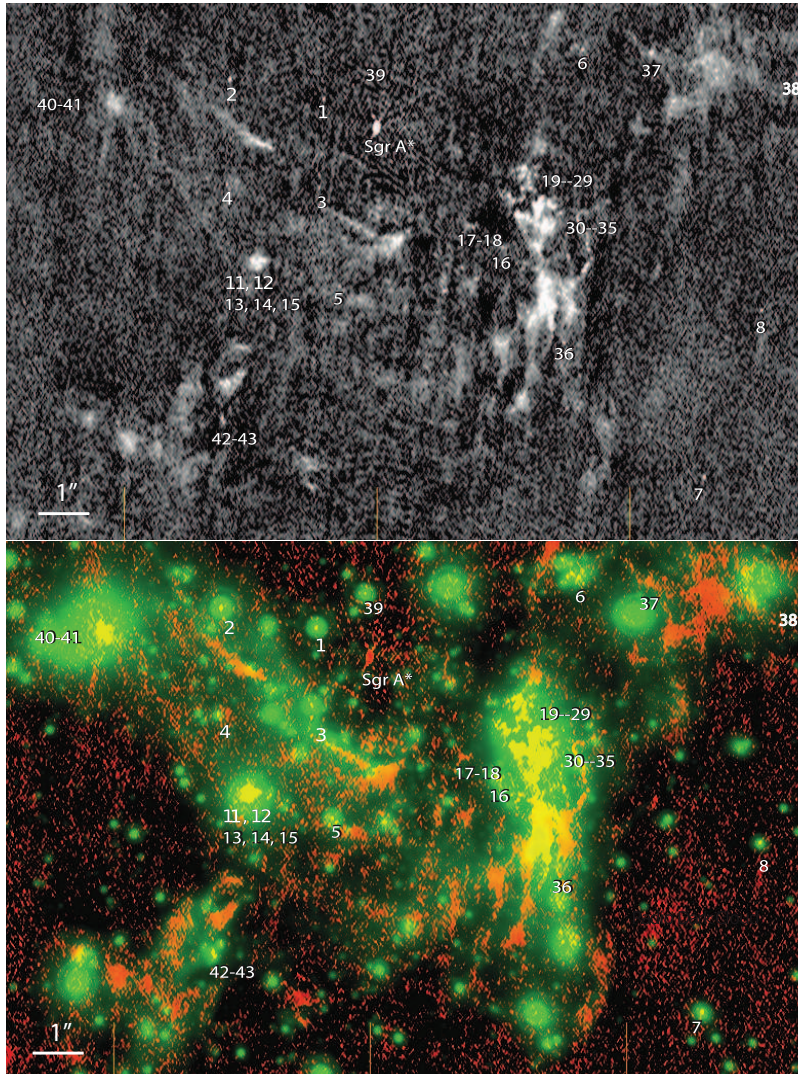


Fig. 1.— (a) A 7 mm continuum image with a resolution of  $82 \times 42$  mas ( $\text{PA} = -5.5^\circ$ ). The effective epoch is August 4, 2011. (b) Same as (a) except a color composite image shows L-band ( $3.8 \mu\text{m}$ ) image in green and a 7 mm image in red.

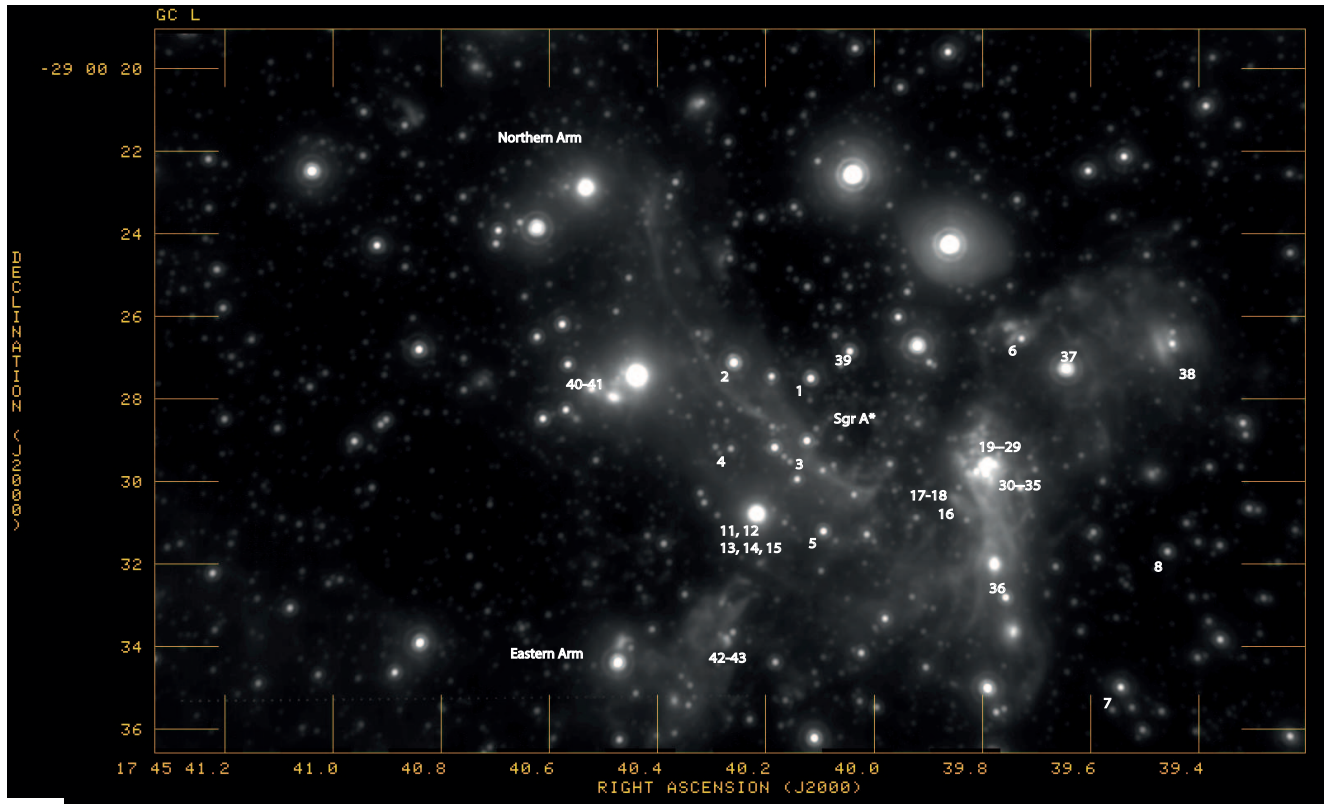


Fig. 2.— A  $3.8\mu\text{m}$  image shows a larger view than presented in Figure 1. All radio stars are labeled except sources 9 and 10 which lie outside the displayed region (see Table 1).

## REFERENCES

- Bower, G. C., Goss, W. M., Falcke, H. *et al.* 2006, ApJ, 648, L127
- Coker, R. F. & Melia, F. 1997, ApJ, 488, L149
- Coker, R. F., Pittaead, J. M. & Kastner, J. H. 2002, A&A, 383, 568
- Contreras, M. E., Rodriguez, L. F., Gomez, Y. & Velazquez, A. 1996, ApJ, 469, 329
- Cuadra, J., Nayakshin, S. & Martins, F. 2008, MNRAS, 383, 458
- Cuadra, J., Nayakshin, S., Springel, V. & Di Matteo, T. 2006, MNRAS, 366, 358
- Eckart, A., Moultaqa, J., Viehmann, T., *et al.* 2004, ApJ, 602, 760
- Eckart, A., Muzic, K., Yazici, S. *et al.* 2013, A&A, 551, A18
- Falcke, H. & Markoff, S. 2009, A&A, 362, 113
- Fritz, T. K., Gillessen, S., Dodds-Eden, K. *et al.* 2010, ApJ, 721, 305
- Genzel, R., Eisenhauer, F. & Gillessen, S. 2010, RvMP, 82, 3121
- Genzel, R., Hollenbach, D. & Townes, C. H. 1994, Reports on Progress in Physics, 57, 417
- Gezari, D., Dwek, E. & Varosi, F. 2003, in Astronomische Nachrichten, Suppl. 1, Proceedings of the Galactic Center Workshop 2002 - The central 300 parsecs of the Milky Way., 573
- Goldston, J. E. and Quataert, E. & Igumenshchev, I. V. 2005, ApJ, 621, 785
- Lacy, J. H., Townes, C. H., Geballe, T. R., & Hollenbach, D. J. 1980, ApJ 241, 132.
- Lang, C. C., Johnson, K. E., Goss, W. M., and Rodriguez, L. F. 2005, AJ, 130, 2185
- Lu, J. R., Ghez, A. M., Hornstein, S. D., Morris, M. R., Becklin, E. E., & Matthews, K. 2009, ApJ, 690, 1463
- Maillard, J. P., Paumard, T., Stolovy, S. R. & Rigaut, F. 2004, A&A, 423, 155M
- Martins, F., Genzel, R., Hillier, D. J. *et al.* 2007, A&A, 468, 233
- Menten, K. M., Reid, M. J., Eckart, A., & Genzel, R. 1997, ApJ, 475, L111
- Muzic, K., Schödel, R., Eckart, A. *et al.* 2008, A&A, 482, 173
- Najarro, F., Krabbe, A., Genzel, R. *et al.* 1997, A&A, 325, 700
- Narayan, R., Yi, I. & Mahadevan, R. 1995, ApJ, 374, L13

- Paumard, T., Genzel, R., Martins, F., Nayakshin, S., Beloborodov *et al.* 2006, ApJ, 643, 1011
- Panagia, N. & Felli, M. 1975, A&A, 39, 1
- Pfuhl, O., Alexander, T., Gillessen, S. *et al.* 2014, ApJ, 782, 101,
- Perger, M., Moulataka, J., Eckart, A., Viehmann, T. *et al.* 2008, A&A, 478, 127
- Quataert, E. 2004, ApJ, 613, 322
- Reid, M. J., Menten, K. M., Genzel, R. *et al.* 2003, ApJ, 587, 208
- Reid, M. J., Menten, K. M., Tripe, S., Ott, T. & Genzel, R. 2007, ApJ, 659, 378
- Roberts, D. A. & Goss, W. M. 1993, ApJS, 86, 133
- Schödel, R., Eckart, A., Iserlohe, C., Genzel, R. & Ott, T. 2005, ApJ, 625, L111
- Serabyn, E. & Lacy, J. H. 1985, ApJ, 293, 445
- Viehmann, T., Eckart, A., Schödel, R. *et al.* 2006, ApJ, 642, 861
- Yusef-Zadeh, F., Royster, M., Wardle, M., *et al.* 2013, ApJ, 767, L32
- Yusef-Zadeh, F., Biretta, J. & Roberts, D. A. 1998, ApJ, 499, L159
- Yusef-Zadeh, F., M., Wardle, M., Roberts, D. A. *et al.* 2014, ApJ, submitted
- Zhao, J.-H., Morris, M., Goss, W. M. & An, T. 2009, ApJ, 699, 186
- Zhao, J.-H. & Goss, W. M. 1998, ApJ, 499, L163

Table 1.

| IR Name                | RA (J2000)<br>(17 <sup>h</sup> 45 <sup>m</sup> ) | Dec (J2000)<br>(−29°00′) | Pos. Accuracy<br>(mas) <sup>†</sup> | Astrometric error<br>(mas) | $\theta_a \times \theta_b$ (PA)<br>mas×mas (deg) | Peak Int.<br>(mJy beam <sup>−1</sup> ) <sup>‡</sup> | Int. Flux<br>(mJy) <sup>‡</sup> | ID |
|------------------------|--|--------------------------|-------------------------------------|----------------------------|--|---|---------------------------------|----|
| Sgr A*                 | 40.0383  | 28.069                   | —                                   | —                          | —  | 2,197.7   | 2,198.8                         | 0  |
|                        | 39.4051  | 27.015                   | —                                   | —                          | —  | 0.49  | 0.37                            | 38 |
| AFNW <sup>§</sup>      | 39.4577  | 31.686                   | 3.4                                 | 8.1                        | —  | 0.73  | 0.56                            | 8  |
| AF <sup>§</sup>        | 39.5440  | 34.980                   | 3.6                                 | 18.1                       | —  | 0.84  | 0.91                            | 7  |
|                        | 39.6239  | 26.602                   | —                                   | —                          | 53×15 (94)                                       | 0.84  | 1.36                            | 37 |
| IRS 34W <sup>§</sup>   | 39.7277  | 26.535                   | 3.3                                 | 11.2                       | —  | 0.77  | 0.62                            | 6  |
|                        | 39.7756  | 31.897                   | —                                   | —                          | 117×43 (7)                                       | 1.24  | 3.18                            | 36 |
| IRS 13E5-f             | 39.7786  | 29.568                   | —                                   | —                          | —  | 1.60  | 2.06                            | 35 |
| IRS 13E3-d             | 39.7941  | 29.617                   | —                                   | —                          | 84×40 (75)                                       | 5.23  | 13.10                           | 33 |
| IRS 13E2-e             | 39.7943  | 29.784                   | —                                   | —                          | 132×66 (5)                                       | 1.56  | 1.67                            | 34 |
| IRS 13N $\gamma$ -j    | 39.7987  | 29.010                   | —                                   | —                          | —  | 0.57  | 0.41                            | 28 |
| IRS 13N-f              | 39.8062  | 29.274                   | —                                   | —                          | —  | 0.85  | 0.66                            | 24 |
| IRS 13N-k              | 39.8075  | 28.985                   | —                                   | —                          | 47×16 (58)                                       | 0.57  | 0.84                            | 29 |
| IRS 13N-g              | 39.8083  | 29.161                   | —                                   | —                          | —  | 0.52  | 0.61                            | 25 |
| IRS 13N-h              | 39.8094  | 29.070                   | —                                   | —                          | —  | 0.50  | 0.46                            | 26 |
| IRS 13E1-a             | 39.8108  | 29.811                   | —                                   | —                          | —  | 0.61  | 0.61                            | 30 |
| IRS 13N-d              | 39.8162  | 29.451                   | —                                   | —                          | —  | 0.65  | 0.98                            | 22 |
| IRS 13E-b              | 39.8171  | 29.831                   | —                                   | —                          | —  | 0.69  | 0.53                            | 31 |
| IRS 13N $\epsilon$ -i  | 39.8173  | 29.030                   | —                                   | —                          | —  | 0.97  | 0.94                            | 27 |
| IRS 13N $\beta$ -e     | 39.8181  | 29.285                   | —                                   | —                          | 77 × 38 (175)                                    | 0.89  | 0.77                            | 23 |
| IRS 13N-c              | 39.8198  | 29.505                   | —                                   | —                          | 76×41 (103)                                      | 1.04  | 2.38                            | 21 |
| IRS 13E-c              | 39.8250  | 29.783                   | —                                   | —                          | 59 × 32 (62)                                     | 1.64  | 3.01                            | 32 |
| X3                     | 39.8478  | 30.445                   | —                                   | —                          | —  | 0.34  | 0.65                            | 16 |
| IRS 13N $\alpha$ -a    | 39.8319  | 29.530                   | —                                   | —                          | —  | 0.74  | 1.11                            | 19 |
| IRS 13N-b              | 39.8382  | 29.426                   | —                                   | —                          | —  | 1.05  | 2.58                            | 20 |
|                        | 39.8927  | 30.045                   | —                                   | —                          | —  | 0.55  | 0.67                            | 17 |
|                        | 39.9004  | 30.016                   | —                                   | —                          | —  | 0.36  | 0.48                            | 18 |
| IRS 16NW <sup>§</sup>  | 40.0451  | 26.847                   | 10.8                                | 28.8                       | —  | 0.39  | 0.27                            | 39 |
| IRS 33E <sup>§</sup>   | 40.0941  | 31.213                   | 5.5                                 | 8.6                        | —  | 0.44  | 0.32                            | 5  |
| IRS 16C <sup>§</sup>   | 40.1177  | 27.513                   | 4.2                                 | 8.0                        | —  | 0.71  | 0.68                            | 1  |
| IRS 16SW               | 40.1245  | 29.018                   | 8.6                                 | —                          | —  | 0.42  | 0.47                            | 3  |
| IRS 21-a               | 40.2095  | 30.696                   | —                                   | —                          | —  | 1.12  | 2.35                            | 11 |
| IRS 21-b               | 40.2183  | 30.845                   | —                                   | —                          | —  | 0.45  | 0.56                            | 12 |
| IRS 21-c               | 40.2194  | 30.742                   | —                                   | —                          | —  | 0.75  | 0.37                            | 13 |
|                        | 40.2254  | 30.718                   | —                                   | —                          | 117 × 57 (16)                                    | 1.06  | 3.28                            | 15 |
| IRS 21-d               | 40.2258  | 30.705                   | —                                   | —                          | —  | 0.88  | 3.13                            | 14 |
| IRS 16NE <sup>§</sup>  | 40.2594  | 27.126                   | 2.2                                 | 9.7                        | —  | 1.32  | 1.22                            | 2  |
| IRS 16SE2 <sup>§</sup> | 40.2637  | 29.200                   | 4.3                                 | 12.9                       | —  | 0.59  | 0.39                            | 4  |
| IRS 1W-a               | 40.4370  | 27.463                   | —                                   | —                          | 73 × 45 (12)                                     | 0.38  | 0.76                            | 40 |
| IRS 1W-b               | 40.4398  | 27.597                   | —                                   | —                          | 19 × 16 (3)                                      | 0.56  | 5.64                            | 41 |
| IRS 5-a                | 40.6938  | 18.268                   | —                                   | —                          | —  | 0.47  | 0.41                            | 9  |
| IRS 5-b                | 40.6956  | 18.179                   | —                                   | —                          | 15 × 11 (8)                                      | 0.49  | 2.85                            | 10 |

<sup>§</sup>radio stars used for astrometry

<sup>†</sup>unless noted, positions are accurate to 25 mas

<sup>‡</sup>15% uncertainty in flux due to scaling to Sgr A\*, which is a variable source

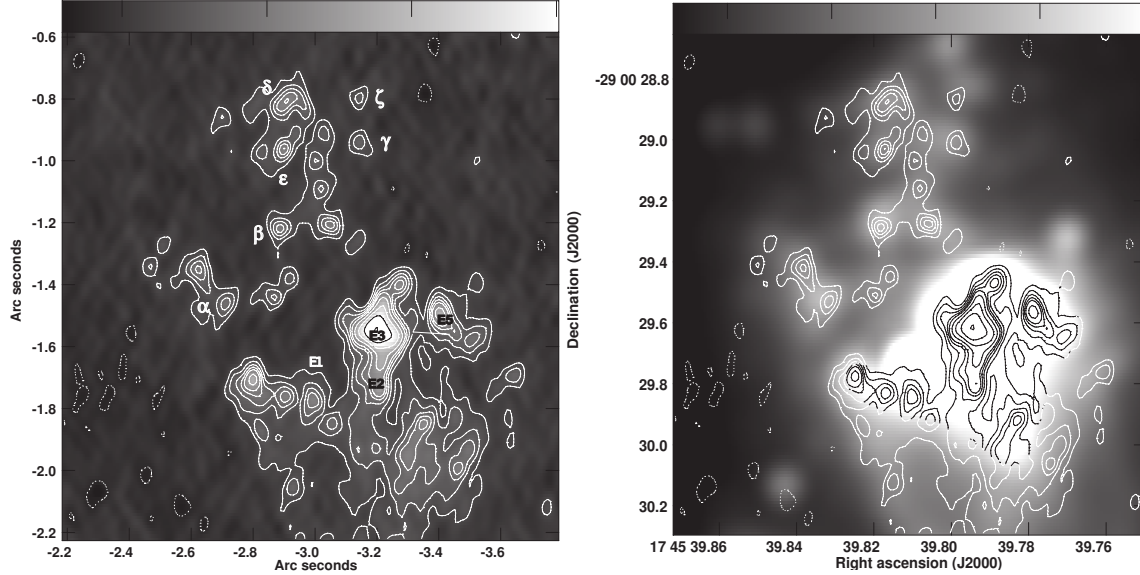


Fig. 3.— (a) A grayscale 7 mm continuum image with an angular resolution of  $82 \times 42$  mas ( $PA = -5.5^\circ$ ). Contour levels are set at  $(-1, 1, 2, 3, 4, 5, 7, 10, 15) \times 0.22 \text{ mJy beam}^{-1}$ . Prominent members of IRS 13E and IRS 13N are labeled. The coordinates are offsets from the position of Sgr A\*. (b) Same as (a) except that contour levels are superimposed on an L-band ( $3.8 \mu\text{m}$ ) image and coordinates are in RA, Dec.

Table 2.

| IR Name   | $\dot{M}$ (Radio)                   | $\dot{M}$ (IR)                      | Integrated Flux | Terminal Velocity |
|-----------|-------------------------------------|-------------------------------------|-----------------|-------------------|
|           | $(10^{-5} M_\odot \text{ yr}^{-1})$ | $(10^{-5} M_\odot \text{ yr}^{-1})$ | $(\text{mJy})$  | $(\text{km/s})$   |
| 34W       | 1.81                                | 1.30                                | 0.61            | 650               |
| IRS 16NW  | 0.90                                | 1.1                                 | 0.27            | 600               |
| IRS 16C   | 1.75                                | 1.1                                 | 0.68            | 650               |
| 33E       | 0.76                                | 2.20                                | 0.32            | 450               |
| AF        | 2.63                                | 1.80                                | 0.91            | 700               |
| AFNW      | 2.10                                | 3.2                                 | 0.56            | 800               |
| IRS 16SE2 | 4.98                                | 7.0                                 | 0.39            | 2500              |
| IRS 16NE  | 3.28                                | —                                   | 1.22            | 700               |
| IRS 16SW  | 1.58                                | —                                   | 0.47            | 700               |